Investigation of Time-of-Flight Benefit for Fully 3-D PET

Suleman Surti* , *Member, IEEE*, Joel S. Karp, *Senior Member, IEEE*, Lucretiu M. Popescu,
Margaret E. Daube-Witherspoon, *Senior Member, IEEE*, and Matthew Werner

Abstract—The purpose of this paper is to determine the benefit that can be achieved in image quality for a time-of-flight (TOF) fully three-dimensional (3-D) whole-body positron emission tomography (PET) scanner. We simulate a 3-D whole-body time-of-flight PET scanner with a complete modeling of spatial and energy resolutions. The scanner is based on $LaBr_3$ Anger-logic detectors with which 300ps timing resolution has been achieved. Multiple simulations were performed for 70-cm long uniform cylinders with 27-cm and 35-cm diameters, containing hot spheres (22, 17, 13, and 10-mm diameter) in a central slice and 10-mm diameter hot spheres in a slice at 1/4 axial FOV. Image reconstruction was performed with a list-mode iterative TOF algorithm and data were analyzed after attenuation and scatter corrections for timing resolutions of 300, 600, 1000 ps and non-TOF for varying count levels. The results show that contrast recovery improves slightly with TOF (NEMA NU2-2001 analysis), and improved timing resolution leads to a faster convergence to the maximum contrast value. Detectability for 10-mm diameter hot spheres estimated using a nonprewhitening matched filter (NPW SNR) also improves nonlinearly with TOF. The gain in image quality using contrast and noise measures is proportional to the object diameter and inversely proportional to the timing resolution of the scanner. The gains in NPW SNR are smaller, but they also increase with increasing object diameter and improved timing resolution. The results show that scan times can be reduced in a TOF scanner to achieve images similar to those from a non-TOF scanner, or improved image quality achieved for same scan times.

Index Terms—Contrast, image quality, $LaBr_3$, lesion detectability, LSO, noise, NPW, time-of-flight PET, TOF.

I. INTRODUCTION

IN the last decade or so, significant effort has been expended in the development of lutetium oxy-orthosilicate (LSO) [1], [2] as a promising scintillator for use in positron emission tomography (PET) [3]. More recently, new lanthanum-based scintillators such as lanthanum bromide ($LaBr_3$) [4], [5] show promise for significant advances in the performance of clinical whole-body PET scanners [6]–[8]. This new generation of PET scintillators is not only very bright (high light output) but is also fast (short decay time) and dense. In addition, the timing

*S. Surti is with the Department of Radiology, University of Pennsylvania, 3400 Spruce Street, Philadelphia, PA 19104 USA (e-mail: surti@mail.med.upenn.edu).

J. S. Karp, L. M. Popescu, M. E. Daube-Witherspoon, and M. Werner are with the Department of Radiology, University of Pennsylvania, Philadelphia, PA 19104 USA.

TABLE I
SCINTILLATION PROPERTIES OF PET SCINTILLATORS

Scintillator	τ (ns)	μ (cm^{-1})	$\Delta E/E$ (%)[a] at 511 keV	Relative light output (%)[b]
NaI(Tl)	230	0.35	6.6	100
BGO	300	0.95	10.2	15
GSO	60	0.70	8.5	25
LSO	50	0.86	10.0	75
$LaBr_3$ (5% Ce)	25	0.47	3.7[c]	175[c]

[a] All energy resolution values are for a large crystal placed directly on PMT.
[b] With respect to NaI(Tl).
[c] An average over different crystal geometries as measured in ou laboratory.

resolution achieved by these scintillators is superior to that achieved by cesium fluoride (CsF) and barium fluoride (BaF_2), two scintillators that were extensively studied in the 1980s for use in time-of-flight (TOF) PET scanners [9]–[11]. The main drawback of CsF and BaF_2 was the low light output and stopping power in comparison to bismuth germanate (BGO), the PET scintillator of choice at that time. The good timing resolution of CsF and BaF_2 compared to BGO, however, allowed the incorporation of TOF information, which partially compensated for their poor spatial resolution and sensitivity compared to BGO scanners. With LSO and $LaBr_3$ it is possible to develop TOF scanners with fewer compromises than those made by the TOF scanners developed in the 1980s [6], [12]–[14]. The TOF measurement, in this situation, will further enhance the high performance expected from these scanners in a conventional non-TOF imaging mode.

Table I summarizes some properties of $LaBr_3$ and LSO together with some other scintillators that have been or are currently of interest in PET.

Previously [8], we have investigated the image quality achieved in a non-TOF $LaBr_3$-based three–dimensional (3-D) whole-body PET scanner for varying scan times and compared it to that for a non-TOF LSO-based 3-D whole-body PET scanner. Image quality was defined using a contrast recovery and noise metric similar to that prescribed in the NEMA NU2-2001 standard for PET scanner performance measurements [15]. Our results showed that despite slightly poorer spatial resolution due to the lower effective-Z of $LaBr_3$, the resultant image quality based upon contrast and noise analysis was similar to that achieved in an LSO scanner for same scan times: slightly better contrast for LSO due to better spatial resolution, but reduced noise for $LaBr_3$ due to better energy resolution and, thus, reduced scatter in the image. In these simulations, the thickness of the $LaBr_3$ crystal and the scanner
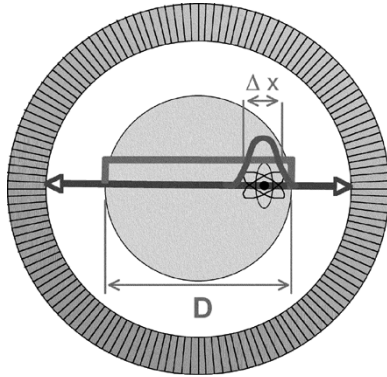
Fig. 1. A schematic diagram of the localization of the emission point along an LOR in a TOF versus non-TOF scanner. In a non-TOF scanner, the reconstruction algorithm assumes that the emission point is uniformly distributed along the LOR. In a TOF scanner the source is more precisely localized within a probability distribution with a spatial FWHM equal to Δx, where $\Delta x = c \bullet \Delta t/2$, c is the speed of light, and Δt is the timing resolution (FWHM) of the scanner.

axial field-of-view were larger than that in the modeled LSO scanner in order to reduce the impact of low sensitivity of $LaBr_3$.

As mentioned earlier, the excellent timing resolution of $LaBr_3$ and LSO provides the capability for developing a TOF capable PET scanner. Our recent measurements with full pixelated Anger-logic detector modules indicate that one can achieve a coincidence timing resolution as good as 300 ps with $LaBr_3$ configured as an Anger-logic detector [7]. In the same work, we also showed that a lutetium-yttrium oxy-orthosilicate (LYSO, similar to LSO) based Anger-logic detector is capable of achieving a coincidence timing resolution of about 600 ps. Similar evaluations for LSO based detector timing resolution for a full scanner have been reported in the range of 800–1200 ps [16].

Fig. 1 is a schematic drawing indicating the localization of the emission point along the line-of-response (LOR) in a TOF versus non-TOF PET scanner. In Fig. 1, D is the object diameter and $\Delta x = c \bullet \Delta t/2$, where c is the speed of light and Δt is the full-width at half-maximum (FWHM) of the timing resolution of the scanner. In a non-TOF scanner, the location of the emission point along the LOR is unknown, so the reconstruction algorithm distributes the counts uniformly along the LOR. In a TOF scanner the source is more precisely localized within a probability distribution with FWHM equal to Δx. This localization leads to reduced noise propagation in the reconstruction algorithm. Previously, it was estimated by *Budinger* that the resultant sensitivity gain is equal to $D/\Delta x$ [17]. Another estimate for sensitivity gain using a variance reduction argument was given by *Tomitani* as being $D/(1.6 \bullet x)$ [18].

The aim of this paper is to investigate through simulations the gain in image quality that can be achieved in a TOF scanner over a non-TOF scanner for different system timing resolutions and count statistics. The image quality measures include estimation of signal-to-noise ratio (SNR) in a lesion detection task using a nonprewhitening matched filter (NPWMF), as well as evaluation of the hot lesion contrast and background noise in reconstructed images.

TABLE II
SCANNER DESIGN PARAMETERS FOR SIMULATIONS

Scintillator	$LaBr_3$
Diameter/Port	84/65 cm
Transverse field-of-view (FOV)	57.6 cm
Axial FOV (AFOV)	25 cm
Lower energy gate (ELLD)	470 keV
Crystal length	30 mm
Coincidence timing window	5 ns

II. EGS4 MONTE CARLO SIMULATIONS

Full scanner simulations were performed using a Monte Carlo tool based upon the EGS4 simulations package [19]. The essential elements of this simulation setup are as follows.

- Cylindrical phantoms are simulated in a cylindrical scanner geometry.
- Coincident photons are emitted within the phantom and their paths traced until they hit the scanner (photoelectric, Compton and Rayleigh scattering used, since photon energies are up to 662 keV).
- A stand alone routine from the *Montecrystal* [20] simulation is used to trace the interactions within the detector, but no scintillation photon tracing is performed.
- The detector point spread function (PSF) (from *Montecrystal* and/or the high count-rate simulation, *HCRSim* [21], [22]) is used for position calculation.
- Emission (and transmission scans) are simulated.
- Scanner shielding is modeled.
- Total, true, single scatter, and multiple scatter list-mode data with time information are simulated and stored separately.

III. SCANNER DESIGN AND PERFORMANCE

For system design simulations the scanner ring and patient port diameters were set at 84-cm and 65-cm, respectively. The annular lead shielding thickness was 2.5-cm. The scanner was simulated as a fully 3-D system without any inter-plane septa. The detector was designed as a discrete crystal Anger-logic detector with the light spread optimized to the area covered by a seven PMT hexagonal cluster. The crystal packing fraction was 86% ($4 \times 4-mm^2$ crystal cross section with a 4.3-mm crystal-to-crystal pitch). Table II gives a summary of other scanner design parameters used in the simulations. The simulated energy resolution for the pixelated Anger-logic detector using $LaBr_3$ was 6.0% at 511 keV which matches measurements taken in our laboratory over several detector modules [7]. The simulated spatial resolution after image reconstruction using filtered backprojection for a point source placed at the center of the FOV was 5.8 mm (FWHM)/13.0 mm full-width at tenth-maximum (FWTM) [8] using NEMA NU2-2001 analysis [15].

Initially, EGS4 simulations were run to estimate the sensitivity and scatter fraction for two uniform cylinders of diameters 27-cm and 35-cm, respectively, and a length of 70-cm. These results, together with those for a 20-cm-diameter, 70-cm-long cylinder, are shown in Table III.

TABLE III
SCATTER FRACTION AND SENSITIVITY RESULTS FOR THE SCANNER DESIGN
STUDIED HERE

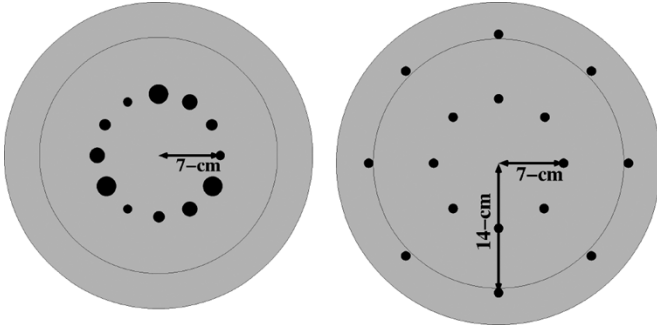|	Sensitivity (kcps/μCi/cc)	Scatter Fraction (%)
20-cm x 70-cm cylinder	1650	18
27-cm x 70-cm cylinder	1840	22
35-cm x 70-cm cylinder	1770	27

Fig. 2. Transverse view of the two slices, Slice A (left) and Slice B (right), containing spherical lesions. The dotted line indicates the boundary or edge of the 27-cm-diameter phantom. Slice A is centered axially in the scanner, while Slice B is at 1/4 the axial FOV from the scanner center.

IV. IMAGE QUALITY PHANTOMS

For this investigation, the simulated phantoms were 70-cm long cylinders with 27-cm and 35-cm diameters. The 27-cm-diameter phantom is more representative of an average clinical patient, while the 35-cm-diameter phantom represents above average or heavy patients [23], [24]. Hot spherical lesions were simulated in 2 different slices. The central slice, Slice A, contained three sets each of 22-mm, 17-mm, 13-mm, and 10-mm diameter spheres, all placed at a radial distance 7 cm from the slice center with an activity uptake ratio of 4:1 with respect to the background [Fig. 2 (left)]. Slice B, at an axial position one-quarter the axial FOV from the center (6.25-cm), contained eight uniformly distributed 10-mm diameter spheres at a radial position of 7-cm [Fig. 2 (right)]. Also, for the 35-cm-diameter cylinder we placed an additional ring of eight 10-mm diameter spheres at a radial position of 14-cm. The activity uptake ratio for these spheres was also 4:1 with respect to the background.

V. LIST-MODE ITERATIVE TOF IMAGE RECONSTRUCTION

A list-mode iterative reconstruction [25], [26] was used for image reconstruction with and without TOF information. The ML-EM type update equation is given by (1), shown at bottom of page, where, λ is the relaxation parameter, Q_j is the sensitivity

of image element j, $x_j^{(n)}$ is the value of image element j for the nth iteration, y_m is the mth event in the list (including crystal pair locations, TOF, and energy), $a_j(y_m)$ is the geometric probability that the detected event y_m came from image element j, $A(y_m)$ and $N(y_m)$ are the attenuation and detector efficiency factors for event y_m, $\tau_j(y_m)$ is the TOF response function, and $R(y_m)$ and $S(y_m)$ are the random and scatter estimates for event y_m. In this paper, scatter corrected true and scatter data with attenuation were reconstructed. Images were generated with attenuation correction performed in the reconstruction algorithm while a lookup table was generated in a model-based single scatter simulation for scatter correction [27] in the reconstruction. Accelerated reconstruction was performed using ten subsets comprising of consecutive (chronologically ordered) events.

VI. SIMULATION SETUP

Simulations were performed for eighteen different sets of data with each set comprising 24 billion positron annihilations. These simulations were repeated for timing resolutions of 300, 600, and 1000 ps as well as non-TOF. Five different collected count statistics (true and scatter counts) were evaluated for each phantom. The collected counts were 3.2, 6.4, 12.8, 25.6, and 35.2 Mcts for the 27-cm-diameter phantom, and 2.1, 4.2, 8.5, 16.9, and 23.2 Mcts in the 35-cm-diameter phantom. Assuming an activity of 3.6 mCi in the phantom, these count levels correspond to scan times of 16, 33, 65, 131, and 180s per bed position for both the phantoms. An activity of 3.6 mCi in the 27-cm-diameter phantom translates into an activity concentration of 0.09 μCi/cc that is similar to clinical activity concentration in average patients at imaging time. The reconstruction time per iteration per Mcts on a single Macintosh G5 2-GHz processor is around 2 min. To run in shorter time we use a multinode computer cluster.

VII. DATA ANALYSIS

Contrast recovery coefficients (CRCs) were calculated in a manner analogous to the NEMA NU2-2001 methodology [15] for the spheres in the center slice (Slice A). CRC is given by

$$\text{CRC} = \frac{\frac{(p_s - p_b)}{p_b}}{c} \tag{2}$$

where p_s is the mean value in an region-of-interest (ROI) centered over the lesion, p_b is an average over the mean values in three background ROIs (4-cm diameter) drawn near the center of the cylinder, and c is the ideal contrast value ($(4-1)/1 = 3$). The average and standard deviation of the CRC value for a given sphere size was then calculated using the three sets of each

$$x_j^{(n+1)} = x_j^{(n)} \left(\frac{1}{Q_j} \times \sum_{m=1}^{M} \frac{a_j(y_m)\tau_j(y_m)A(y_m)N(y_m)}{\sum_{k=1}^{J} a_k(y_m)\tau_k(y_m)A(y_m)N(y_m)x_k^{(n)} + R(y_m) + S(y_m)} \right)^{\lambda} \tag{1}$$
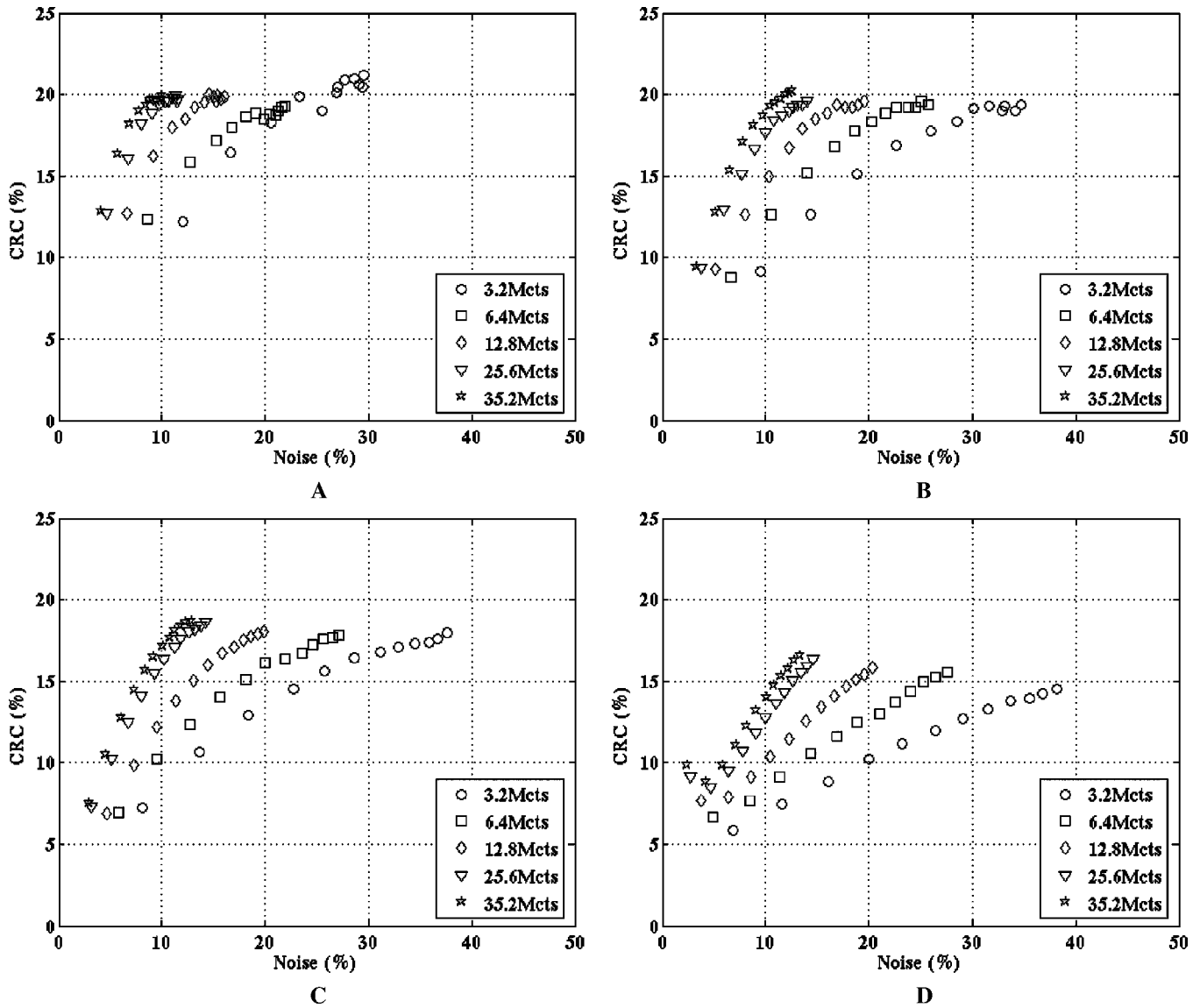
Fig. 3. CRC versus noise plot for the 10-mm-diameter sphere in the center slice (Slice A) of the 27-cm-diameter phantom: (A)–(C) for TOF scanners with timing resolutions of 300, 600, and 1000 ps, respectively, while (D) is for a non-TOF scanner. The points along each curve for a constant timing resolution and count statistic are for increasing number of iterations in the reconstruction, starting with iteration 1 on lower left.

sphere in each of the eighteen noise realizations, leading to a total of 54 different realizations. Noise was estimated as the ratio of the standard deviation of counts to the mean counts per pixel in each of the background ROIs. The reported number is the average over the 54 different realizations.

Also, lesion detectability for a signal known exactly and background known exactly (SKE/BKE) task was estimated using a NPWMF and data for the 10-mm spheres (Slice B) [28], [29]. The NPWMF is a linear observer, and its observer response variable λ_i is given by the scalar (dot) product

$$\lambda_i = (\langle f_1 \rangle - \langle f_0 \rangle) \bullet f_i \tag{3}$$

where f_i is a sample reconstructed image and $\langle f_i \rangle$ is the ensemble mean, for the ith class with $i = 1$ for signal present

class and $i = 0$ for signal absent class of images. Lesion detectability or NPW SNR is then defined as

$$\text{NPW SNR} = \frac{\langle \lambda_1 \rangle - \langle \lambda_0 \rangle}{\sqrt{\frac{1}{2} \left(\sigma_1^2 + \sigma_0^2 \right)}} \tag{4}$$

where $\langle \lambda_i \rangle$ is the mean of the observer response variable of the ith class and σ_i^2 its corresponding variance. For the target present class, a square template of 21 pixels wide (4.2-cm) was placed around each of the eight spheres in Slice B (care was taken so that the individual templates did not overlap), as well as the eighteen different noise realizations, giving a total of 144 realizations for the signal present class. For signal absent class the process was repeated with the templates placed at the exact same positions as the spheres, but in a slice in the same axial position but opposite to Slice B ($z = -6.25$ cm) [23], [30], [31].
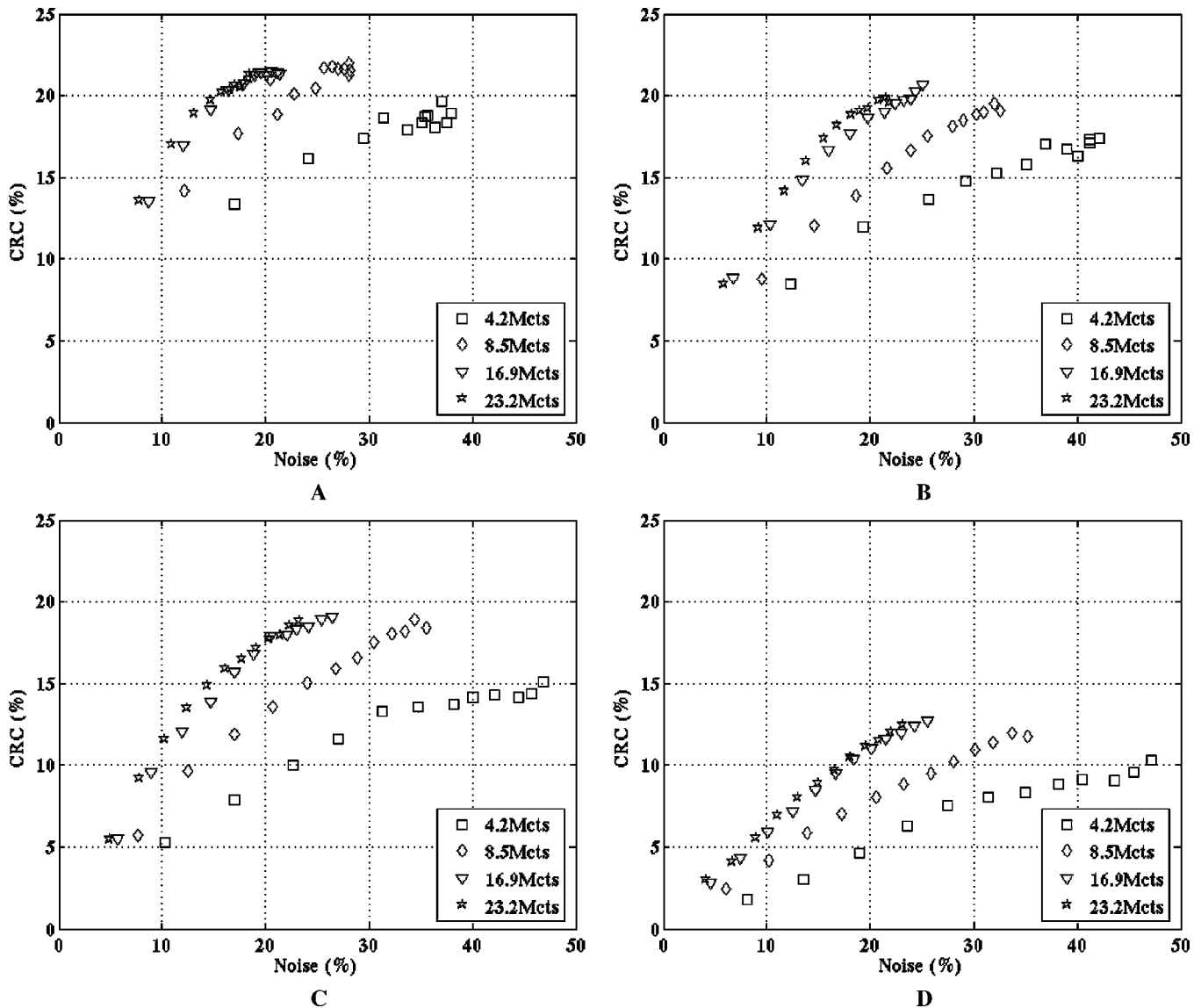
Fig. 4. CRC versus noise plot for the 10-mm diameter sphere in the center slice (Slice A) of the 35-cm-diameter phantom: (A)–(C) for TOF scanners with timing resolutions of 300, 600, and 1000 ps, respectively, while (D) is for a non-TOF scanner. The points along each curve for a constant timing resolution and count statistic are for increasing number of iterations in the reconstruction, starting with iteration 1 on lower left.

Error estimation was performed using standard error propagation techniques [32].

VIII. RESULTS

A. CRC and Noise

Figs. 3 and 4 show the CRC values for the 10-mm sphere in the central slice (Slice A) as a function of noise in the background for different timing resolutions and varying count statistics in the 27-cm- and 35-cm-diameter phantoms. The points along each curve for a constant timing resolution and count statistic correspond to increasing numbers of iterations in the reconstruction, from 1 to 12. As expected, noise in each of these plots decreases as the scan time or collected counts is increased. As the timing resolution improves, the images achieve the maximum CRC value for fewer iterations. For example, in Fig. 3(a) for 300 ps, a maximum CRC value of about 20% is achieved in

5–6 iterations. In contrast, in Fig. 3(d) for non-TOF, a CRC of only 15%–17% is achieved after 12 iterations, indicating slower convergence for the non-TOF reconstruction. A similar conclusion is derived from the data for the 35-cm phantom as shown in Fig. 4, although convergence is slower with this larger phantom.

In Fig. 5, we overlay selected plots for CRC versus Noise, picking a count statistic or scan time for a fixed timing resolution in the 27-cm-diameter phantom. The plot shows that the curves for 6.4 Mcts with 300-ps timing resolution, 12.8 Mcts with 600 ps timing resolution, and 35.2 Mcts with non-TOF are very similar to each other and are close to overlapping. We did not attempt to optimize the overlap by fine tuning the statistics of each data set. This indicates that better timing resolution leads to similar CRC/noise characteristics as in a poorer timing resolution scanner but with fewer counts (shorter scan time). The expected gain in sensitivity using the $D/\Delta x$ relation gives factors of 6 and 3, respectively, for 300- and 600-ps TOF scanners
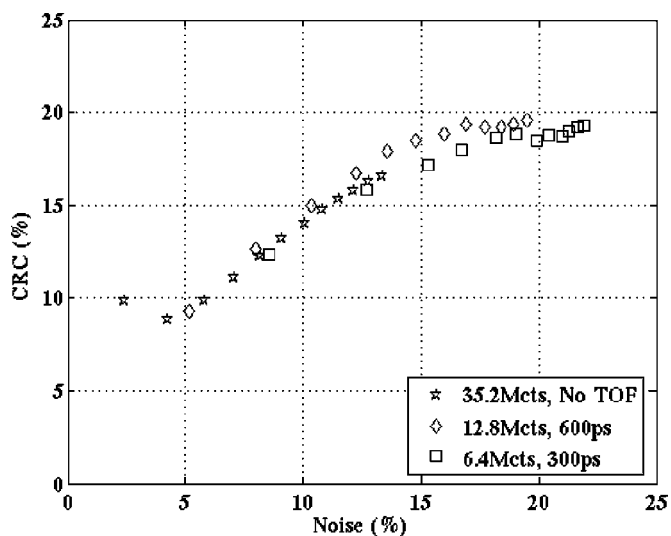
Fig. 5. Summary plot of CRC versus noise for the 10-mm diameter sphere in the center slice (Slice A) of the 27-cm-diameter phantom. The three curves are extracted for varying count statistics (or scan times) with different timing resolutions in a TOF or a non-TOF scanner as shown earlier in Fig. 3. The relative overlap of these curves indicates that good timing resolution in a TOF scanner leads to similar image quality as in a non-TOF scanner but with reduced counts or scan time. Note that better CRC is achieved with less iterations as the timing resolution improves.
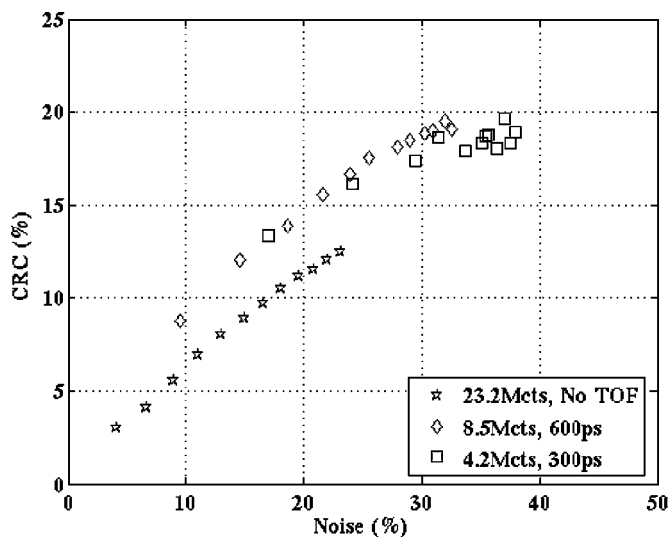

Fig. 6. Summary plot of CRC versus noise for the 10-mm diameter sphere in the center slice (Slice A) of the 35-cm-diameter phantom. The three curves are extracted for varying count statistics (or scan times) with different timing resolutions in a TOF or a non-TOF scanner as shown earlier in Fig. 4. The relative overlap of these curves indicates that good timing resolution in a TOF scanner leads to similar or better image quality as in a non-TOF scanner but with reduced counts or scan time. Note that better CRC is achieved with less iterations as the timing resolution improves.

over the non-TOF scanner. The curves in Fig. 5 are in reasonable agreement with this, since the 300 ps curve has half the number of counts as the 600-ps curve and slightly more than six times the number of counts in the non-TOF scanner. Similar results are obtained for the 35-cm-diameter phantom as shown in Fig. 6. The expected gain in sensitivity based on $D/\Delta x$ is now 7.8 and 3.9, respectively, for the 300- and 600-ps timing resolution compared to the non-TOF scanner. The curve for 300

ps once again overlaps with the 600-ps curve but with half the number of counts, while the non-TOF curve does not match this performance with about 5.5 times the number of counts with 300-ps timing resolution.

Fig. 7 shows the central slices from representative images for the 27-cm-diameter phantom. These correspond to similar noise properties (about 12%) in images with 6.4 Mcts for 300 ps, 12.8 Mcts for 600 ps, 25.6 Mcts for 1000 ps, and 35.2 Mcts for non-TOF. The images look very similar visually, indicating that a 300-ps TOF scanner can achieve similar image quality in 1/6 the scan time as non-TOF scanner and with few iterations in reconstruction.

In Fig. 8, we show the central slices from representative images for the 27-cm-diameter phantom for a fixed number of counts (6.4 Mcts) and CRC value (about 17%). The CRC value of about 17%, achieved after 12 iterations in a non-TOF scanner [see Fig. 3(d)], was used to select the TOF images. As is clear from Fig. 3(a)–(c) the TOF scanner can achieve better CRC values than those shown in these images by increasing the number of iterations. In Fig. 8, it is clear that improved timing resolution in a TOF scanner leads to reduced noise in the reconstructed images with fewer iterations for a fixed scan time.

B. Lesion Detectability—NPW SNR

In Fig. 9, we plot the lesion detectability as measured using the NPW SNR metric for a matched filter. The detectability measure was calculated for the 10-mm diameter spheres in the off-center slice (Slice B) of the two phantoms. The NPW SNR values reach a constant value after the first few (2–5) iterations of image reconstruction for all timing resolutions as well as non-TOF. For lesion detection tasks a maximum NPW SNR value is desired and five iterations of image reconstruction achieves this for all timing resolutions as well as non-TOF. Hence, five iterations were used for all plots shown in Fig. 9. For the 35-cm-diameter phantom the results are shown for the inner ring of spheres (radial position of 7-cm). The results for the outer ring of spheres (radial position of 14-cm) in the 35-cm-diameter phantom show similar behavior with about a 10% overall increase in the NPW SNR compared to the inner ring of spheres in the same phantom. These plots indicate that lesion detectability increases nonlinearly as a function of count statistics and timing resolution. Additionally, the gain in lesion detectability with TOF does not change significantly as a function of radial position in the large phantom. In Figs. 10 and 11, we show representative images for Slice B in the 27-cm- and 35-cm-diameter phantoms, respectively, for non-TOF and 300-ps TOF scanners. Recall that the count levels for the two phantoms were initially chosen to correspond to equal scan times. Three scan times corresponding to count statistics of 12.8, 25.6, and 35.2 Mcts in the 27-cm phantom and 8.5, 16.9, and 23.2 Mcts in the 35-cm phantom, are shown. For the non-TOF scanner the spheres are not clearly visible in the 35-cm-diameter phantom even after collecting 23.2 Mcts. On the other hand, for a 300-ps timing resolution TOF scanner, the spheres are reasonably well visualized after collecting 16.9 Mcts. In particular, the sphere detectability in the 35-cm phantom with 300-ps TOF scanner is similar to the sphere detectability in the 27-cm phantom in a non-TOF scanner

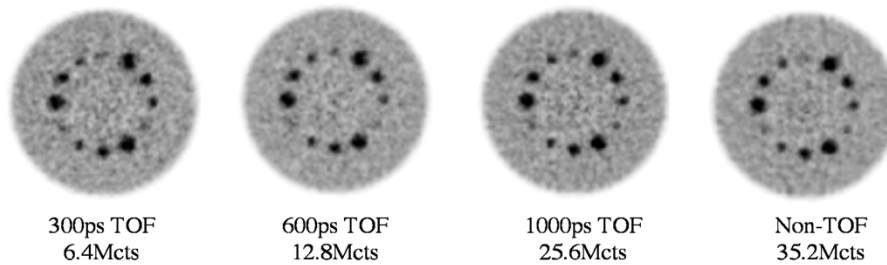| 300ps TOF | 600ps TOF | 1000ps TOF | Non-TOF |
| 6.4Mcts | 12.8Mcts | 25.6Mcts | 35.2Mcts |

Fig. 7. Reconstructed images for the central slice (Slice A) in the 27-cm phantom. These images are for varying count statistics or scan times, but similar noise values (about 12% as shown in Fig. 3). Moving left to right the images are: 300-ps TOF scanner with 6.4 Mcts, 600 ps TOF scanner with 12.8 Mcts, 1000 ps TOF scanner with 25.6 Mcts, and non-TOF scanner with 35.2 Mcts. Improved timing resolution in a TOF scanner leads to similar image quality but with reduced counts or scan time.

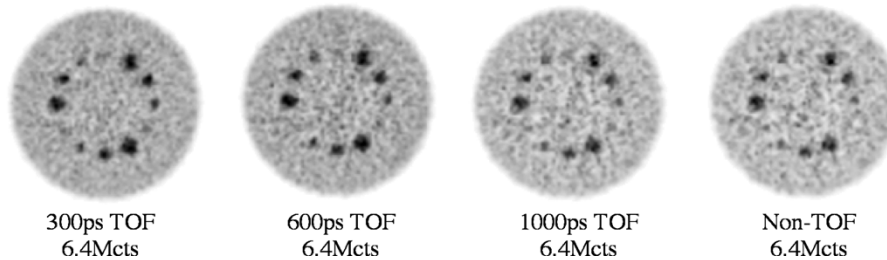| 300ps TOF | 600ps TOF | 1000ps TOF | Non-TOF |
| 6.4Mcts | 6.4Mcts | 6.4Mcts | 6.4Mcts |

Fig. 8. Reconstructed images for the central slice (Slice A) in the 27-cm phantom. These images are for a fixed count statistics (6.4 Mcts) and similar CRC (about 17% as shown in Fig. 3). Moving left to right the images are: 300 ps TOF scanner, 600-ps TOF scanner, 1000-ps TOF scanner, and non-TOF scanner. Same scan times lead to improved image quality in a TOF scanner with better timing resolution.
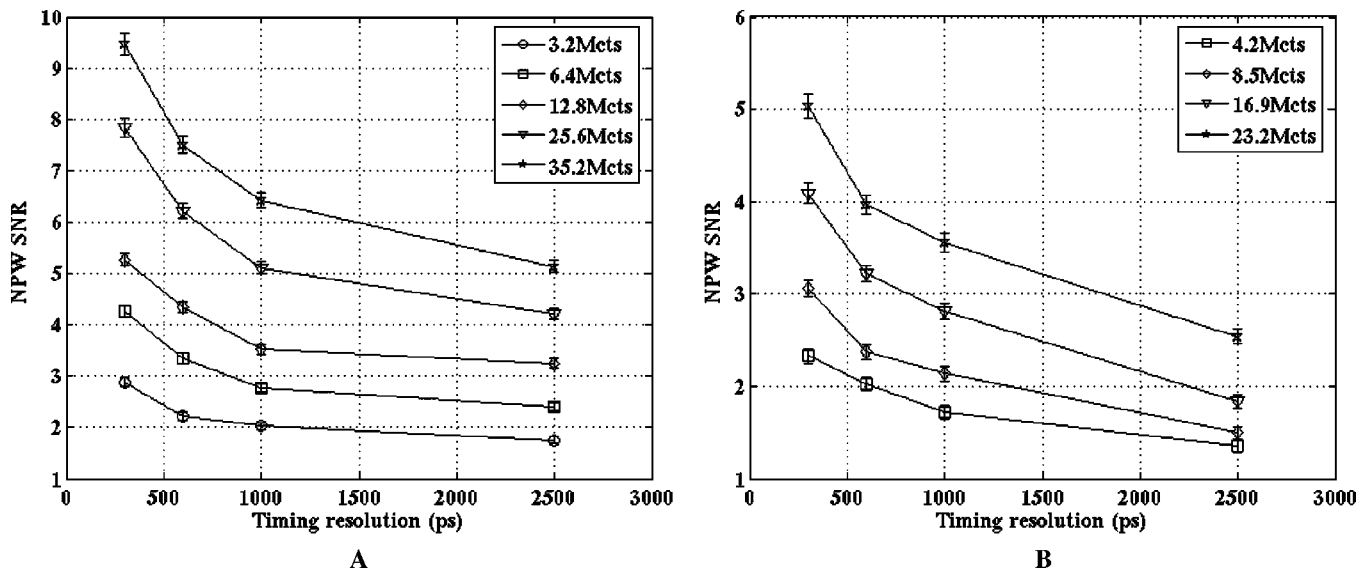

Fig. 9. Lesion detectability as measured by the NPW SNR for the 10-mm spheres in Slice B at a radial position of 7-cm from the center of the phantom: (A),(B) for the 27-cm- and 35-cm-diameter phantoms, respectively. The points at 2500-ps timing resolution are for a non-TOF scanner. Recall that the count levels for the two phantoms when moving for high to low correspond to equal scan times, i.e., 35.2 Mcts in (A) corresponds to the same scan time as 23.2 Mcts in (B) and onwards.

when scanning for the same imaging time. These results can also be deduced from the plots in Fig. 9.

IX. DISCUSSION AND CONCLUSION

The CRC plots shown in Figs. 3 and 4 indicate faster convergence (fewer iterations) of the reconstruction with better timing resolution. The non-TOF scanner converges very slowly to a CRC value that is slightly lower than that for a TOF scanner with 300-ps timing resolution. Fig. 5 shows that CRC and noise

values for a TOF scanner with 300-ps timing resolution are similar to those in a 600-ps TOF scanner, but these are achieved with half the counts of the 600-ps data. A 300-ps TOF scanner compared to a non-TOF scanner achieves similar or better image quality with only 1/6 the total counts. From Fig. 6 for the 35-cm-diameter phantom we reach similar conclusions. However, the image quality in the non-TOF scanner is still noticeably worse (increased noise for same CRC value) compared to the 300-ps TOF scanner even with six times the total counts. These results indicate that there is an equivalent sensitivity gain of six for the
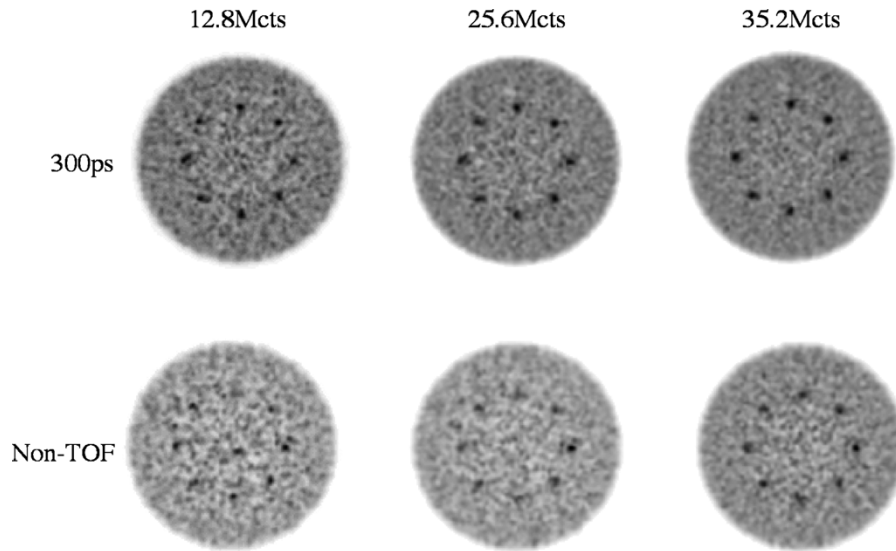
Fig. 10. Reconstructed images for Slice B in the 27-cm phantom. The top row is for a TOF scanner with 300-ps timing resolution while the bottom row is for a non-TOF scanner. Moving left to right, these are 12.8-, 25.6-, and 35.2-M counts in the images.
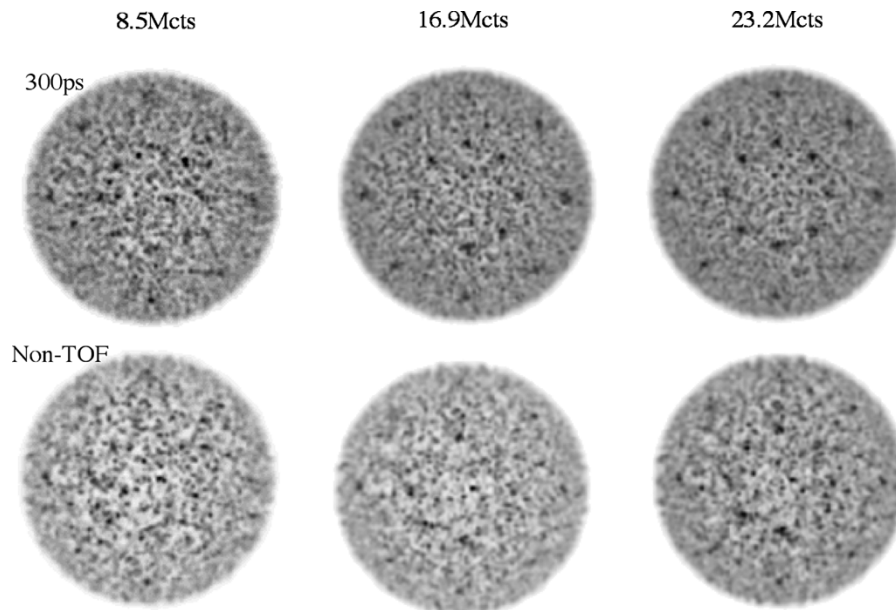

Fig. 11. Reconstructed images for Slice B in the 35-cm phantom. The top row is for a TOF scanner with 300-ps timing resolution while the bottom row is for a non-TOF scanner. Moving left to right, these are 8.5 M, 16.9 M, and 23.2 M counts in the images.

27-cm-diameter phantom, and greater than six for the 35-cm-diameter phantom, in a 300-ps TOF scanner over a conventional non-TOF scanner. These results are in reasonable agreement with the previously calculated gain in sensitivity expected from a TOF scanner and given by $D/\Delta x$ (6.0 and 7.8, respectively).

The results for lesion detectability as measured by the NPW SNR metric, indicate that there is a noticeable improvement in the detection of small lesions with low uptake ratios with improved timing resolution in a TOF scanner. This gain, which increases with larger phantom diameter, does not, however, scale as the square root of $D/\Delta x$ but is a smaller factor that is closer to another derivation derived from variance reduction principles by *Tomitani* $(D/(1.6\bullet\Delta x))$ [18]. In addition, the gain in NPW SNR as a function of timing resolution is spatially invariant, as seen

with the 35-cm cylinder. The lesion detectability results show that with a 300-ps TOF scanner detectability in a heavy (35-cm diameter) patient is similar to that obtained with a non-TOF scanner for an average patient (27-cm diameter). This is especially important when we consider the fact that even with 23 Mcts (180-s "scan"), the smaller 10-mm spheres are not visible in the 35-cm phantom for a non-TOF scanner, while a 300-ps TOF scanner provides reasonable detection with only 17 Mcts (130-s "scan"). Therefore, a TOF scanner can achieve similar image quality to that of a non-TOF scanner with reduced scan times; conversely, for similar scan times, image quality is significantly improved in a TOF scanner.

The gains in image quality for the TOF scanner are summarized in Table IV which also includes the two theoretical mea-

TABLE IV
GAIN IN IMAGE QUALITY FOR TOF SCANNERS WITH DIFFERENT TIMING RESOLUTION S OVER NON-TOF SCANNERS

	27 x 70-cm phantom			35 x 70-cm phantom		
	300ps	600ps	1000ps	300ps	600ps	1000ps
Sensitivity gain, D/Δx	6.0	3.0	1.8	7.8	3.9	2.3
Variance reduction, D/(1.6·Δx)	3.8	1.9	1.1	4.9	2.4	1.4
Equal CRC and noise	5.5	2.8	> 1.4	> 5.6	> 2.8	> 1.4
(NPW SNR)^2	(3.1)[a] 2.7-3.4	(1.9) 1.6-2.2	(1.4) 1.2-1.6	(4.0) 3.0-4.9	(2.6) 2.3-3.1	(2.0) 1.6-2.3

[a]The range is over the different count statistics while the number in () is an average value over them.

sures of expected gain, defined previously [17], [18]. The gain from equal CRC and noise are difficult to quantify due to the dependence of these values on the iteration number. We estimated the gain in this measure of image quality by determining the overlap between CRC/noise curves for varying count statistics and timing resolutions from Figs. 5 and 6, and within the limits of the choices made for both statistics and timing resolution. For this reason some of the expected gains shown in row 5 of Table IV could only be approximated (eg. >1.4 for 1000-ps with 27-cm-diameter phantom). The gains observed with the CRC and noise measure are similar to those predicted by the D/Δx relationship. However, the gains from NPW SNR are lower but consistently increase with better timing resolution and large phantoms.

These investigations included the effects of both scatter and attenuation in the object. Another factor that affects image quality in PET imaging and that increases in significance with increasing activity in the phantom is random coincidences. In the future we plan to evaluate the changes in image quality of a TOF scanner as a function of activity level. Besides changing random coincidences in the phantom, increased activity levels can also lead to increased scatter and worsened spatial resolution in the scanner due to pulse pileup effects. With improved timing resolution there also exists the possibility of applying a timing gate (maximum allowed difference in arrival times of coincident photons) to the collected data based on the object size, just as the use of an energy gate is used to reduce scatter in conventional non-TOF scanners. Our simulations suggest that for 300-ps timing resolution, reducing the coincidence timing window from 5 ns to 2 ns leads to a reduction in the scatter fraction from 22% (for 27-cm × 70-cm cylinder) to 17% without reducing the true coincidences. A bigger impact is observed in random coincidences, which are reduced by about 55% from the total random coincidences collected over the entire scanner FOV. For example, with 3.6 mCi in the 27-cm-diameter phantom the randoms fraction (random coincidences divided by true and scatter coincidences) is reduced from 0.60 to about 0.28. All these factors will be folded in the simulations to evaluate the count-rate behavior of images obtained in TOF-capable LSO and LaBr$_3$ scanners. Eventually we intend to perform some of these image quality measurements on a prototype TOF scanner we are currently developing at our institute.

REFERENCES

[1] C. L. Melcher and J. S. Schweitzer, "A promising new scintillator—cerium-doped lutetium oxyorthosilicate," *Nucl. Instrum. Meth. Phys. Res. A*, vol. 314, pp. 212–214, 1992.

[2] ——, "Cerium-doped lutetium oxyorthosilicate: a fast, efficient new scintillator," *IEEE Trans. Nucl. Sci.*, vol. 39, no. 4, pp. 502–505, Aug. 1992.

[3] R. Nutt, "Is LSO the future of PET? for," *Eur. J. Nucl. Med.*, vol. 29, pp. 1523–1525, 2002.

[4] E. V. D. van Loef, P. Dorenbos, C. W. E. van Eijk, K. Kramer, and H. U. Gudel, "High-energy-resolution scintillator: Ce3+ activated LaBr3," *Appl. Phys. Lett.*, vol. 79, pp. 1573–1575, 2001.

[5] K. S. Shah, J. Glodo, M. Klugerman, W. W. Moses, S. E. Derenzo, and A. J. Weber, "LaBr3: Ce scintillators for gamma-ray spectroscopy," *IEEE Trans. Nucl. Sci.*, vol. 50, no. 6, pp. 2410–2413, Dec. 2003.

[6] S. Surti, J. S. Karp, G. Muehllehner, and P. S. Raby, "Investigation of lanthanum scintillators for 3-D PET," *IEEE Trans. Nucl. Sci.*, vol. 50, no. 3, pp. 348–354, Jun. 2003.

[7] A. Kuhn, S. Surti, J. S. Karp, P. S. Raby, K. S. Shah, A. E. Perkins, and G. Muehllehner, "Design of a lanthanum bromide detector for time-of-flight PET," *IEEE Trans. Nucl. Sci.*, vol. 51, no. 5, pp. 2550–2557, Oct. 2004.

[8] S. Surti, J. S. Karp, and G. Muehllehner, "Image quality assessment of LaBr3-based whole-body 3D PET scanners: a Monte Carlo evaluation," *Phys. Med. Biol.*, vol. 49, pp. 4593–4610, 2004.

[9] R. Allemand, C. Gresset, and J. Vacher, "Potential advantages of a cesium fluoride scintillator for a time-of-flight positron camera," *J. Nucl. Med.*, vol. 21, pp. 153–155, 1980.

[10] M. Ter-Pogossian, D. Ficke, M. Yamamoto, and J. T. Hood, "Super PETT I: a positron emission tomograph utilizing photon time-of-flight information," *IEEE Trans. Nucl. Sci.*, vol. NS-1, pp. 179–187, 1982.

[11] W. H. Wong, N. A. Mullani, G. Wardworth, R. K. Hartz, and D. Bristow, "Characteristics of small barium fluoride (BaF_2) scintillator for high intrinsic resolution time-of-flight positron emission tomography," *IEEE Trans. Nucl. Sci.*, vol. NS-31, pp. 381–386, 1984.

[12] W. W. Moses and S. E. Derenzo, "Prospects for time-of-flight PET using LSO scintillator," *IEEE Trans. Nucl. Sci.*, vol. 46, no. 3, pp. 474–478, Jun. 1999.

[13] W. W. Moses, "Time of flight in PET revisited," *IEEE Trans. Nucl. Sci.*, vol. 50, no. 5, pp. 1325–1330, Oct. 2003.

[14] T. K. Lewellen, "Time-of-flight PET," *Sem. Nucl. Med.*, vol. 28, pp. 268–275, 1998.

[15] NEMA Standards Publication NU 2-2001, "Performance Measurements of Positron Emission Tomographs," National Electrical Manufacturers Association. Rosslyn, VA, 2001.

[16] M. Conti, B. Bendriem, M. E. Casey, M. Chen, F. Kehren, C. Michel, and V. Panin, "Implementation of time-of-flight on CPS HiRez PET scanner," presented at the 2004 IEEE Nuclear Science Symposium and Medical Imaging Conf., Rome, Italy, 2004.

[17] T. F. Budinger, "Time-of-flight positron emission tomography—status relative to conventional PET," *J. Nucl. Med.*, vol. 24, pp. 73–76, 1983.

[18] T. Tomitani, "Image-reconstruction and noise evaluation in photon time-of-flight assisted positron emission tomography," *IEEE Trans. Nucl. Sci.*, vol. NS-28, pp. 4582–4589, 1981.

[19] L. E. Adam, J. S. Karp, and G. Brix, "Investigation of scattered radiation in 3D whole-body positron emission tomography using Monte Carlo simulations," *Phys. Med. Biol.*, vol. 44, pp. 2879–2895, 1999.

[20] J. S. Karp and G. Muehllehner, "Performance of a position-sensitive scintillation detector," *Phys. Med. Biol.*, vol. 30, pp. 643–655, 1985.

[21] D. A. Mankoff, G. Muehllehner, and J. S. Karp, "The high count rate performance of a two-dimensionally position-sensitive detector for positron emission tomography," *Phys. Med. Biol.*, vol. 34, pp. 437–456, 1989.

[22] S. Surti, "A model of scintillation detector performance for positron emission tomography," Ph.D. dissertation, Univ. Pennsylvania, Philadelphia, PA, 2000.

[23] S. Surti, R. D. Badawi, C. H. Holdsworth, G. El Fakhri, P. E. Kinahan, and J. S. Karp, "A multi-scanner evaluation of PET image quality using phantom studies," presented at the 2003 IEEE Nuclear Science Symp. Medical Imaging Conf., Portland, OR, 2003.

[24] P. E. Kinahan, S. Surti, R. D. Badawi, G. El Fakhri, J. S. Karp, and T. K. Lewellen, "Effect of patient thickness on noise equivalent count rates for 2D and fully-3D whole-body PET imaging," *J. Nucl. Med.*, vol. 45, pp. 102P–103P, 2004.

[25] L. M. Popescu, "Iterative image reconstruction using geometrically ordered subsets with list-mode data," presented at the 2004 IEEE Nuclear Science Symp. Medical Imaging Conf., Rome, Italy, 2004.

[26] L. M. Popescu and R. M. Lewitt, "Tracing through a grid of blobs," presented at the 2004 IEEE Nuclear Science Symp. Medical Imaging Conf., Rome, Italy, 2004.

[27] R. Accorsi, L.-E. Adam, M. E. Werner, and J. S. Karp, "Optimization of a fully 3D single scatter simulation algortihm for 3D PET," *Phys. Med. Biol.*, vol. 49, pp. 2577–2598, 2004.

[28] H. H. Barrett, J. Yao, J. P. Rolland, and K. J. Myers, "Model observers for assessment of image quality," *PNAS*, vol. 90, pp. 9758–9765, 1993.

[29] P. F. Judy, R. G. Swensson, and M. Szulc, "Lesion detection and signal-to-noise ratio in CT images," *Med. Phys.*, vol. 8, pp. 13–23, 1981.

[30] S. C. Moore, G. El Fakhri, R. D. Badawi, A. D. Van den Abbeele, and R. E. Zimmerman, "Relative lesion detectability in 3D vs 2D dedicated multi-ring PET," presented at the 2000 IEEE Nuclear Science Symp. Medical Imaging Conf., Lyons, France, 2000.

[31] G. El Fakhri, R. D. Badawi, S. Surti, C. H. Holdsworth, P. E. Kinahan, J. S. Karp, and T. K. Lewellen, "Is noise equivalent count rate a good surrogate of lesion detectability in whole-body PET?," *J. Nucl. Med.*, vol. 45, p. 164P, 2004.

[32] C. K. Abbey, H. H. Barrett, and M. P. Eckstein, "Practical issues and methodology in assessment of image quality using model observers," *Proc. SPIE*, vol. 3032, Medical Imaging 1997: Physics of Medical Imaging, pp. 182–194, May 1997.